Available online at www.sciencedirect.com
ScienceDirect
Trans. Nonferrous Met. Soc. China 30(2020) 2274−2282
Transactions of Nonferrous Metals Society of China
www.tnmsc.cn

Isothermal reduction kinetics of zinc calcine under carbon monoxide

Yu-jie CHEN[1], Yun-yan WANG[1,2], Ning PENG[1,2,3], Yan-jie LIANG[1,2], Bing PENG[1,2]

1. Institute of Environmental Science and Engineering, School of Metallurgy and Environment, Central South University, Changsha 410083, China;
2. Chinese National Engineering Research Center for Control & Treatment of Heavy Metal Pollution, Changsha 410083, China;
3. School of Materials Science and Engineering, Central South University, Changsha 410083, China

Received 23 April 2019; accepted 28 June 2020

Abstract: The reduction kinetics of zinc calcine under a CO atmosphere was evaluated by isothermal reductive roasting in a temperature range of 600−800 °C. The extent of reaction of zinc calcine was measured using thermogravimetry (TG), and the decomposition mechanism of zinc ferrite in zinc calcine was analyzed based on variations in the soluble zinc and ferrous contents. The results indicate that the reaction was controlled by the nucleation of the products, with an apparent activation energy of 65.28 kJ/mol. The partial pressure of CO affected the reaction rate more strongly than the CO intensity (defined as $P_{CO}/(P_{CO}+P_{CO_2})$). The generation rate of zinc oxide was higher than that of ferrous oxide; therefore, the nucleation of ferrous oxide is the rate-determining step of the reaction.
Key words: reduction kinetics; zinc calcine; zinc ferrite; carbon monoxide

1 Introduction

Due to the depletion of zinc ores, the use of high iron-bearing resources has received increasing attention [1]. Zinc ferrite is generated as a byproduct of the desulfurization roasting of high iron-bearing zinc ores, resulting in not only heavy metal contamination but also the waste of resources [1,2]. The reduction roasting process, as a common method of solid-waste treatment [3,4], has been found to be a productive means of decomposing zinc ferrite in high iron-bearing zinc calcines. Nevertheless, a systematic kinetic investigation is still warranted because the reaction is slow.

Previous studies on reduction kinetics have emphasized the reduction kinetics of iron oxides because of the importance of iron and steel in both current and future technologies [5]. Hundreds of such reports have appeared in *Web of Science* over the past five decades. These studies can be used as references for research methodologies. Nonetheless, because of differences in the lattice structures of iron oxide and zinc ferrite, these reports do not precisely describe the reduction mechanism of zinc ferrite.

In the view of these issues, many researchers have studied the reduction kinetics of zinc ferrite. WANG et al [6] investigated the carbothermic reduction of zinc ferrite under microwave heating. The reduction mechanism was primarily controlled by the gasification of carbon, and the apparent activation energy was 38.21 kJ/mol. STOPIC and FRIEDRICH [7] studied the decomposition kinetics of zinc ferrite and determined that the chemical control process, which had an activation energy of 166.9 kJ/mol, was the rate-determining step. LEE

Foundation item: Projects (2018YFC1903301, 2018YFC1900301) supported by the National Key Research and Development Program of China; Project (51825403) supported by the National Natural Science Foundation for Distinguished Young Scholars of China
Corresponding author: Ning PENG; Tel: +86-731-88830577; E-mail: 201761@csu.edu.cn
DOI: 10.1016/S1003-6326(20)65378-X

et al [8] performed the carbothermal reduction of zinc ferrite in the temperature range of 800−1200 °C. The results showed that zinc ferrite was first decomposed into zinc oxide and hematite, which were subsequently reduced. The rate-determining step was the diffusion of the gas products, and the overall rate of reaction increased when the argon flow rate was increased or the size of the carbon agglomerates decreased [8]. JUNCA et al [9,10] analyzed the reduction of zinc ferrite and electric arc furnace dust pellets in a gas mixture of CO and H_2. Their study revealed that the reduction of zinc ferrite could be separated into two steps: the first step is controlled by both two-dimensional nucleation and one-dimensional diffusion, whereas the second step is controlled by a mixture of two- and three-dimensional diffusion and reaction. The reduction mechanism of electric arc furnace dust pellets was similar to that of zinc ferrite. The diffusion of zinc ions in the solid phase was also reported to be the rate-determining step when zinc ferrite was reduced in CO or H_2 [11−13]. In our previous study, a differential method was used to investigate the reduction kinetics of zinc ferrite under nonisothermal conditions [14]. However, achieving the selective reduction of zinc ferrite to produce zinc oxide and magnetite requires the use of a mixture of CO and CO_2 gas as the reducing agent. The effect of introducing CO_2 on the reduction rate remains to be studied.

In addition, in industrial applications, zinc ferrite is embedded in zinc oxide because zinc oxide is the main phase in zinc calcine. The complex internal structure of zinc calcine grains compared with that of pure zinc ferrite might result in more complicated mechanisms, which requires further study. The present work highlights the reduction kinetics of zinc calcine in CO. The effects of the reaction parameters on the reaction rate are quantitatively described by their exponent in kinetic equations. In addition, new evaluation indicators for studying the formation rates of iron and zinc oxide in high iron-bearing zinc calcines during the reduction process are defined.

2 Experimental

2.1 Materials

Zinc calcine was obtained from a zinc plant located in Inner Mongolia, China. The sample was dried, ground and sieved to a particle size between 45 and 74 μm before the roasting experiments. The elemental composition is given in Table 1. The grades of zinc and iron were 57.37% and 14.96%, respectively. The X-ray diffraction (XRD) pattern of the zinc calcine is shown in Fig. 1. Zinc oxide, zinc ferrite and zinc silicate were determined to be the main zinc phases in the zinc calcine, and lead sulfate was also detected.

Table 1 Chemical composition of zinc calcine obtained by XRF (wt.%)

Zn	Fe	O	Pb	Si
57.37	14.96	16.58	2.49	1.77
S	Cu	Mn	Al	Mg
0.53	0.91	0.69	0.25	0.46
Ca	Ba	Co	P	Ra
0.15	0.12	0.07	0.05	0.01

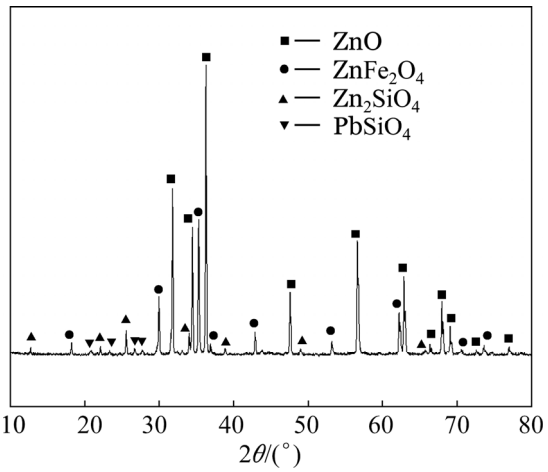

Fig. 1 XRD pattern of zinc calcine

2.2 Experimental procedure

The experiments were performed in a NETZSCH STA 449F3 apparatus capable of thermogravimetry−differential scanning calorimetry (TG−DSC) analysis in the temperature range from 25 to 1650 °C, as shown in Fig. 2. 20 mg zinc calcine was directly reduced in corundum pans under a gas flow of 100 mL/min in each experiment. The heating process consisted of two steps. In the first step, the samples were heated to the desired temperature at a heating rate of 30 °C/min under an Ar flow, and in the second step, the isothermal TG curves were obtained in the temperature range of 600−800 °C under a gas

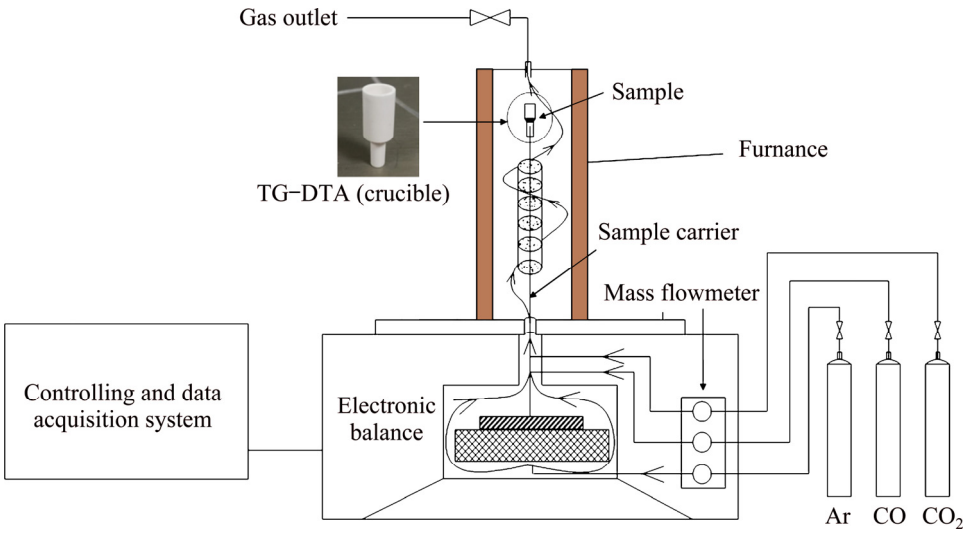

Fig. 2 Schematic diagram of TG analyzer

mixture of CO, CO_2 and Ar. The partial pressures of CO and CO_2 were controlled by adjusting the gas flow with a mass flow controller.

X-ray fluorescence (XRF) spectroscopy (ZSX Primus II) was performed to quantitatively analyze the elements in the high iron-bearing zinc calcine. The phase transformation during the roasting process was analyzed by XRD using Cu K_α radiation (Rigaku, TTR-III).

2.3 Kinetic analysis

To obtain the kinetic parameters of the reduction roasting process, a series of isothermal experiments were performed. The kinetic equation can be written as

$$G(\alpha)=k(T)t \tag{1}$$

where $G(\alpha)$ is the integral form of the reaction model, and the dependence of k on T can be written as

$$k(T)=A\cdot\exp\left(-\frac{E_a}{RT}\right) \tag{2}$$

To evaluate the effects of the partial pressure of CO (P_{CO}) and CO intensity (defined as $P_{CO}/(P_{CO}+P_{CO_2})$, represented by V_{CO}) on the reaction rate, the pre-exponential factor A is defined as

$$A=C\cdot P_{CO}^{n}\cdot V_{CO}^{m} \tag{3}$$

where n and m are the exponents of P_{CO} and V_{CO}, respectively, and C is a constant. Combining Eqs. (1), (2) and (3) gives

$$G(\alpha)=C\cdot P_{CO}^{n}\cdot V_{CO}^{m}\cdot\exp\left(-\frac{E_a}{RT}\right)\cdot t \tag{4}$$

From Eq. (4), the following equation is obtained:

$$\ln\frac{G(\alpha)}{t}=\ln\left[C\cdot\exp\left(-\frac{E_a}{RT}\right)\right]+n\ln P_{CO}+m\ln V_{CO} \tag{5}$$

The mechanism equation can be obtained by the model matching method, and E_a can then be evaluated using Eq. (2). The E_a was assumed to be a function only of temperature. The first term on the right side of Eq. (5) is constant at a fixed temperature, and n and m can be calculated by the linear fitting of the experimental data obtained from single-factor experiments.

3 Results and discussion

3.1 Reductive decomposition of zinc calcine

Based on the main phase composition of the zinc calcine, the possible reactions that occur during its selective reduction roasting by CO are

$$3ZnFe_2O_4+CO=3ZnO+2Fe_3O_4+CO_2 \tag{6}$$

$$ZnFe_2O_4+CO=ZnO+FeO+CO_2 \tag{7}$$

$$ZnFe_2O_4+2CO=Zn+2FeO+2CO_2 \tag{8}$$

$$ZnFe_2O_4+4CO=Zn+2Fe+4CO_2 \tag{9}$$

$$Fe_3O_4+CO=3FeO+CO_2 \tag{10}$$

Figure 3(a) shows the Gibbs free energy changes of these reactions in the temperature range

of 0−1000 °C at a CO intensity of 20% and a partial pressure of CO of 8%. As shown in Fig. 3(a), zinc ferrite was reduced to zinc oxide and magnetite by CO over entire temperature range (ΔG of Eq. (6) is negative). The ΔG for the generation of ferrous oxide and zinc metal is positive (Eqs. (7)−(9)), which means that magnetite and zinc oxide are stable below 1000 °C. The TG curve of zinc oxide obtained under a reductive atmosphere is shown in Fig. 3(b). Two mass-loss steps were observed between ambient temperature and 900 °C. The first step was caused by the evaporation of water, and the second step was due to the reduction of zinc oxide. A slight mass loss was observed at 900 °C, which is consistent with previous reports [15−17].

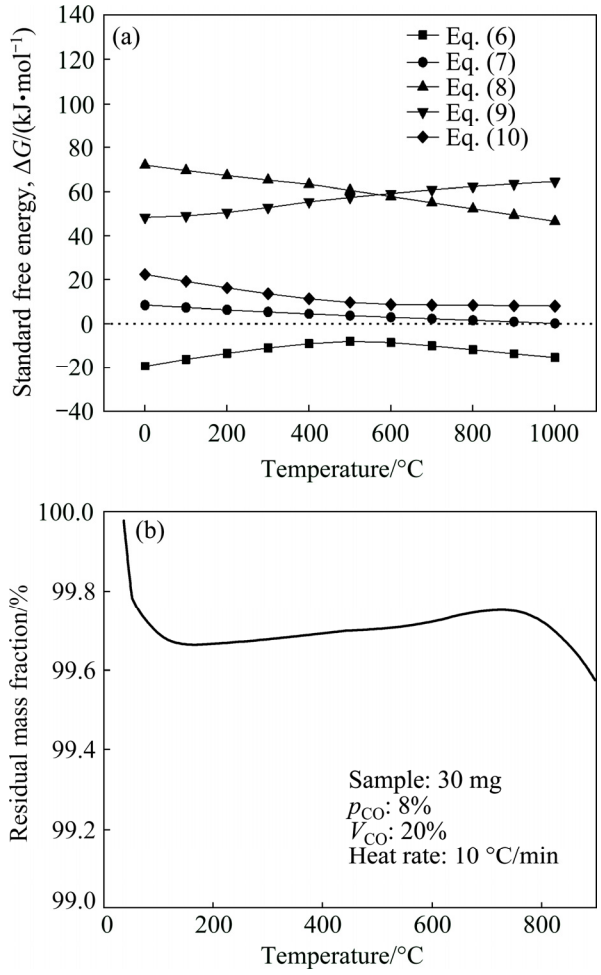

Fig. 3 Standard free energy changes for reduction of zinc ferrite by carbon monoxide in temperature range of 0−1000 °C (a) and TG curve of nonisothermal reduction process of zinc oxide (b)

Figure 4 shows the isothermal TG−DTG curves for the reductive roasting of the high iron-bearing zinc calcine using a gas mixture of CO, CO_2 and Ar. The temperature influences both the reaction rate and reaction extent, as shown in Figs. 4(a) and (b). The results in Figs. 4(c) and (d) were obtained by fixing the partial pressure of CO at 8% and the temperature at 700 °C. The effect of the CO intensity on the reaction rate is negligible at the beginning of the reaction, as demonstrated by the near overlap of the TG and DTG curves in the first few minutes. The TG curves separate after 30 min of reductive roasting, which is consistent with the results of our previous study [18], where the over-reduction extent (i.e., the extent to which magnetite in the roasted product was further reduced to ferrous oxide) of zinc ferrite increased with increasing CO intensity. As shown in Figs. 4(e) and (f), the partial pressure of CO mainly affects the reaction rate but not the reaction extent at a CO intensity of 20% and 700 °C. All the curves show that the reaction rate is maximal at the beginning of the reaction and rapidly decreases with increasing reaction time; this decrease is correlated with a change in the reaction mechanism.

3.2 Calculation of kinetic triplet

The most common rate equations for solid-state reactions are summarized in Table 2 [19]. The most likely mechanism function $G(\alpha)$ was determined using model-fitting methods, in which linear regressions between the experimentally measured and calculated reaction extent data were performed. The extent of reaction ranged from 0 to 1 and was calculated from the TGA data using Eq. (11):

$$\alpha = \frac{m_0 - m_t}{m_0 - m_e} \tag{11}$$

where m_t represents the mass of the sample at time t, and m_0 and m_e are the masses of the sample at the beginning and end of the process, respectively. All mass values were expressed as the residual mass fraction. According to Fig. 4(a), m_0 is 100%; a value of 97.25% was chosen for m_e.

The fitting results are shown in Table 2. The 6th model has the highest correlation coefficient R for multiple data sets obtained at different temperatures. Therefore, $G(\alpha)=[-\ln(1-\alpha)]^{3/2}$ is the most likely mechanism function, and the linear fitting results are depicted in Fig. 5(a). This model is an Avrami−Erofeev-type model, indicating that the reaction was mainly controlled by nucleation

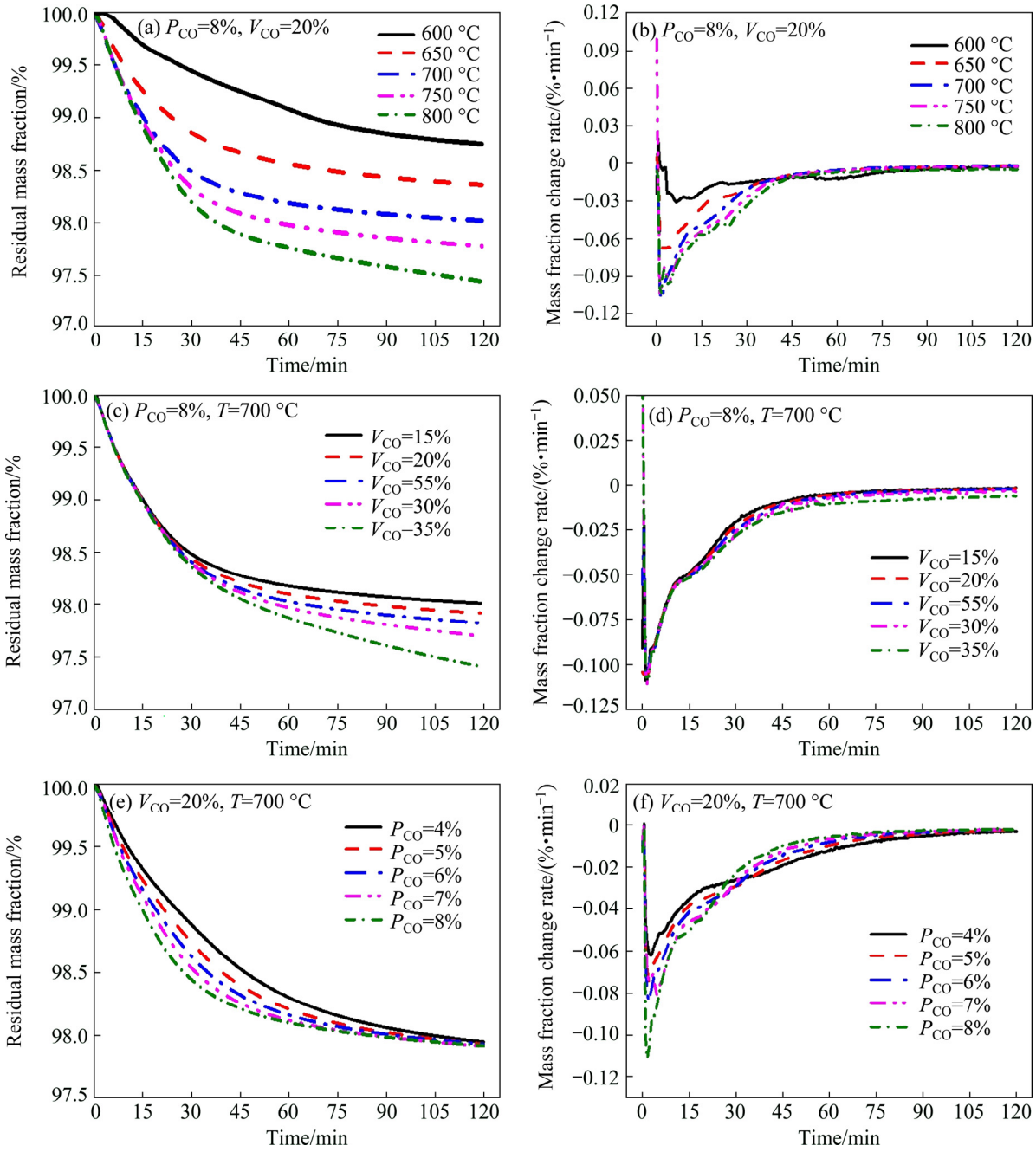

Fig. 4 TG (a, c, e) and DTG (b, d, f) curves of isothermal reduction process of zinc calcines roasted at different temperatures (a, b), CO intensities (c, d) and partial pressures of CO (e, f)

and growth of the roasted products, with an apparent reaction order of 1.5. The apparent activation energy E_a was calculated to be 65.28 kJ/mol, as shown in Fig. 5(b).

The data sets in Figs. 4(c) and (e) were used to calculate the exponents of V_{CO} and P_{CO} in Eq. (5) based on the reaction model $G(\alpha)=[-\ln(1-\alpha)]^{3/2}$. The values of $\ln k$ versus $\ln V_{CO}$ and $\ln P_{CO}$ were plotted in Fig. 6, and the $\ln V_{CO}$ data obtained at a P_{CO} value of 8% and 700 °C were fitted. The V_{CO} value and temperature for the fitting of $\ln P_{CO}$ were 20% and 700 °C, respectively. The exponent of $\ln V_{CO}$ and $\ln P_{CO}$ were determined to be 0.12 and 0.73, respectively, suggesting that P_{CO} is more critical than V_{CO} for accelerating the reaction. Although the numerical values of these factors are special cases of this study, this conclusion is an important reference for the kinetic analysis of the carbothermal reduction of other metal oxides. Combining the fitting results in Figs. 5 and 6 gives

Table 2 Important rate equations used for solid-state kinetics and linear fittings

No.	Reaction model	Code	$G(\alpha)$	R_{600}	R_{650}	R_{700}	R_{750}	R_{800}	R_{AVG}
1	Three-dimensional diffusion (Z−L−T equation)	−	$[(1-\alpha)^{-1/3}-1]^2$	0.9942	0.9984	0.9964	0.9961	0.9943	0.9959
2	Three-dimensional diffusion (Jander equation)	D3	$[1-(1-\alpha)^{1/3}]^2$	0.9923	0.9977	0.9965	0.9928	0.9871	0.9933
3	Three-dimensional diffusion (G−B equation)	D4	$1-2\alpha/3-(1-\alpha)^{2/3}$	0.9936	0.9983	0.9967	0.9953	0.9924	0.9952
4	Growth of nuclei (A−E equation)	A_1	$-\ln(1-\alpha)$	0.9945	0.9882	0.9892	0.9962	0.9992	0.9934
5	Growth of nuclei (A−E equation)	A_2	$[-\ln(1-\alpha)]^{1/2}$	0.9608	0.9489	0.9571	0.9704	0.9806	0.9636
6	Growth of nuclei (A−E equation)	−	$[-\ln(1-\alpha)]^{3/2}$	0.9994	0.9988	0.9976	0.9969	0.9926	0.9970
7	Growth of nuclei (A−E equation)	AE2	$[-\ln(1-\alpha)]^2$	0.9903	0.9960	0.9946	0.9869	0.9760	0.9888
8	Growth of nuclei (A−E equation)	AE3	$[-\ln(1-\alpha)]^3$	0.9562	0.9744	0.9751	0.9562	0.9351	0.9594
9	Growth of nuclei (A−E equation)	AE4	$[-\ln(1-\alpha)]^4$	0.9170	0.9463	0.9497	0.9235	0.8951	0.9263
10	Contracting cylinder	R2	$1-(1-\alpha)^{1/2}$	0.9921	0.9811	0.9797	0.9884	0.9938	0.9870
11	Contracting sphere	R3	$1-(1-\alpha)^{1/3}$	0.9929	0.9837	0.9832	0.9915	0.9964	0.9896
12	Phase boundary reaction−Mampel Power	F1	$-\ln(1-\alpha)$	0.9945	0.9882	0.9892	0.9962	0.9992	0.9934
13	Two order	F2	$(1-\alpha)^{-1}$	0.9979	0.9972	0.9985	0.9973	0.9888	0.9959
14	Three order	F3	$(1-\alpha)^{-2}$	0.9995	0.9997	0.9962	0.9822	0.9569	0.9869

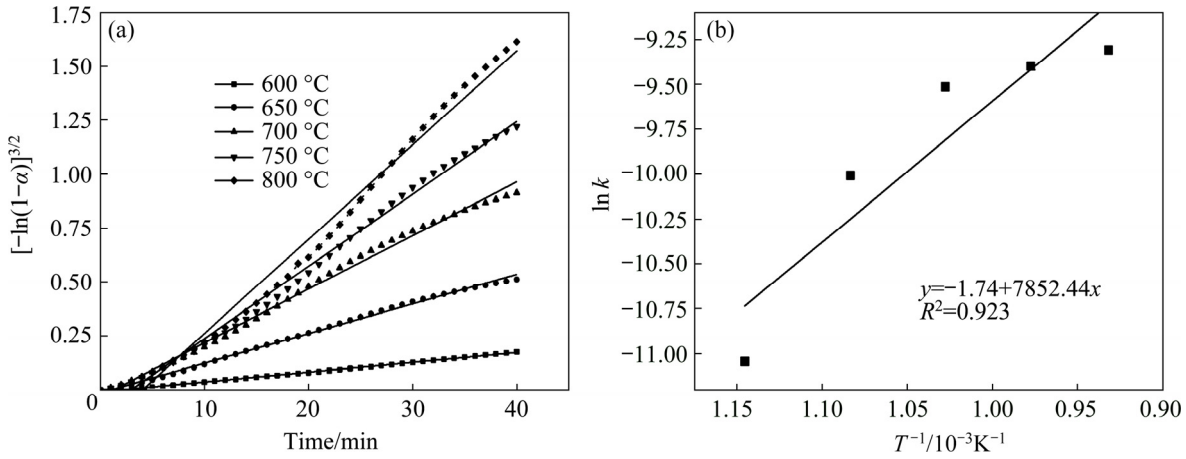

Fig. 5 Experimental data and kinetic fitting curves for zinc calcine roasted at different temperatures (a) and Arrhenius diagram used to calculate apparent activation energy (b)

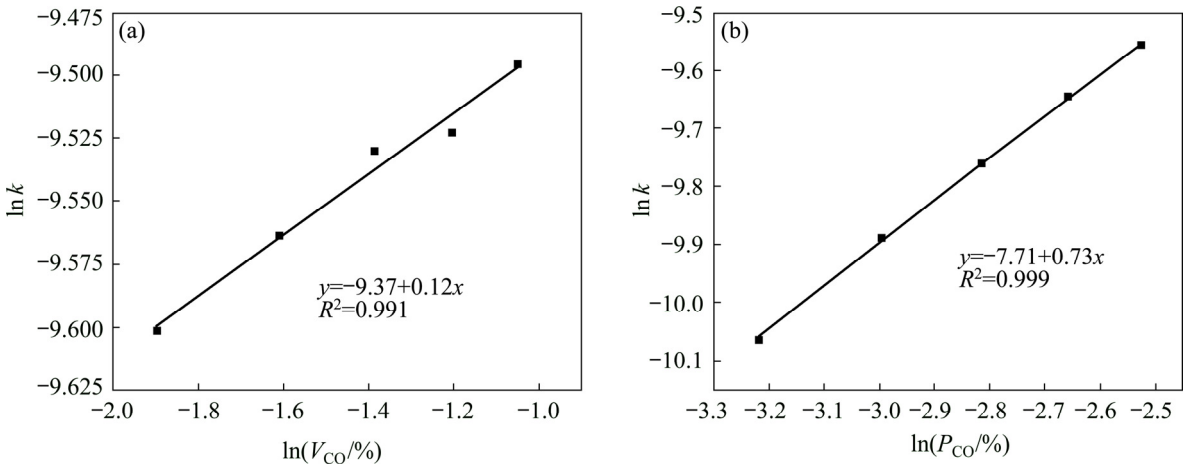

Fig. 6 Linear fitting results of ln k versus ln V_{CO} (a) and ln k versus ln P_{CO} (b)

the following kinetic equation:

$$[-\ln(1-\alpha)]^{3/2} = 1.726P_{CO}^{0.73} \cdot V_{CO}^{0.12} \cdot \exp\left(-\frac{6.53\times10^4}{RT}\right) \cdot t \quad (12)$$

where the units of activation energy, temperature and time are J/mol, K and min, respectively. Notably, this equation is derived from fitting the experimental data obtained at a CO intensity of 15%−35%, a CO partial pressure of 4%−8%, and a temperature of 600−800 °C. Therefore, it is not necessarily applicable to data obtained under other experimental conditions.

3.3 Kinetic analysis of reduction process

Because of the complex phase composition of zinc calcines, obtaining quantitative information about the phase transformation during the reduction of zinc ferrite is difficult. In our previous studies, the soluble zinc and the ferrous contents were used to evaluate the extent of reaction. The reduction of zinc ferrite results in increases in the soluble zinc and ferrous contents, which correspond to the generation of zinc oxide and ferrous oxide, respectively. The theoretical molar ratio of the increase in the ferrous content to the increase in the soluble zinc is 2:1 based on the stoichiometric elemental composition of zinc ferrite. To determine the relative formation rates of zinc oxide and ferrous oxide quantitatively, N was defined as

$$N = \frac{\Delta n_F}{\Delta n_Z} = \frac{(w_t^F - w_0^F)/M_F}{(w_t^Z - w_0^Z)/M_Z} \quad (13)$$

where Δn_F and Δn_Z are the changes in the amount of ferrous oxide and zinc oxide, respectively; w_t^F and w_t^Z are the ferrous and soluble zinc contents, respectively, at time t; w_0^F and w_0^Z are the initial ferrous and soluble zinc contents, respectively; and M_F and M_Z are the molar masses of iron and zinc, respectively.

The zinc calcine was roasted in a tube furnace under a weakly reducing atmosphere [20]. The soluble zinc and ferrous contents of the roasted product are shown as a function of time in Figs. 7(a)

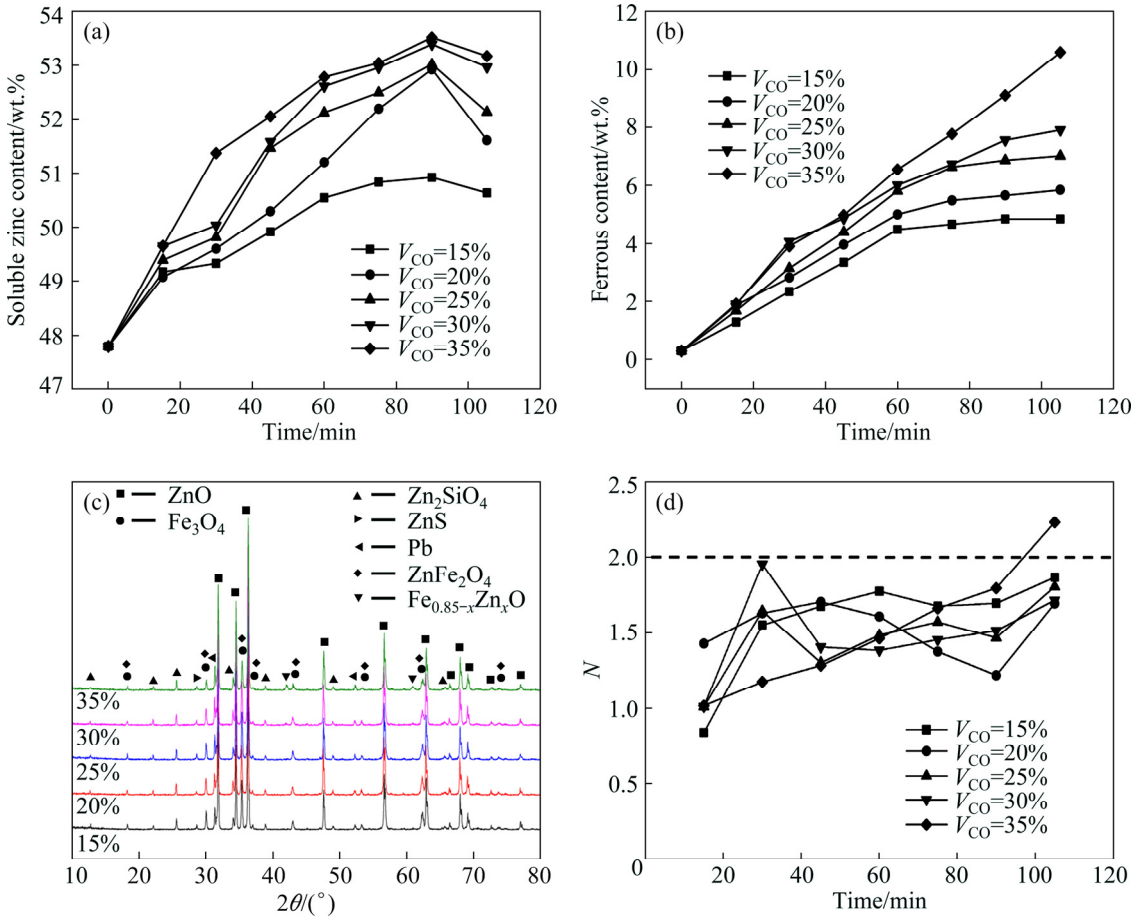

Fig. 7 Variations in soluble zinc (a) and ferrous (b) contents versus time; XRD patterns of zinc calcine roasted at different CO intensities (c); N value as a function of time (d) at P_{CO} value of 8% and 700 °C

and (b), respectively. Figure 7(a) shows that soluble zinc reaches a maximum after 105 min of roasting and then decreases with increasing time. Meanwhile, the ferrous content continues to increase under the same conditions, as shown in Fig. 7(b). The decrease in soluble zinc was due to the generation of a zinc−iron solution ($Fe_{0.85-x}Zn_xO$), as shown in Fig. 7(c). Moreover, the characteristic peaks of this solid solution were only detected in the roasted product at a CO intensity of 35%. The N value in Fig. 7(d) is less than 2, which means that the increase in the ferrous content is lower than the theoretical value. Moreover, the formation of zinc oxide was faster than that of ferrous oxide due to the presence of a large amount of zinc oxide in the zinc calcine, which provides abundant nucleation centers and accelerates the nucleation of zinc oxide. Therefore, the nucleation of ferrous oxide or other low-valence iron oxides is the rate-determining step.

4 Conclusions

(1) The reductive roasting kinetics of zinc ferrite in zinc calcines were analyzed using the isothermal reduction method. Model fitting was performed using linear regression methods, and $G(\alpha)=[-\ln(1-\alpha)]^{3/2}$ represents the most likely mechanism function.

(2) The apparent activation energy and the reaction orders of the partial pressure of CO and CO intensity were evaluated based on the obtained reaction model. The exponent of P_{CO} is greater than that of V_{CO}, indicating that P_{CO} affects the reaction rate more significantly than V_{CO}. The nucleation of ferrous oxide is found to be the rate-determining step.

(3) It is demonstrated that the exponents of the partial pressure of CO and CO intensity could be obtained through appropriately designed thermo-gravimetric reduction experiments and that the relative effects of these two parameters on the reaction kinetics could be quantitatively compared based on their reaction orders.

(4) The integration methods employed in this work can only be applied to the kinetic analysis of the entire reduction process.

References

[1] HOLLOWAY P C, ETSELL T H, MURLAND A L. Use of secondary additives to control the dissolution of iron during Na_2CO_3 roasting of La Oroya zinc ferrite [J]. Metallurgical and Materials Transactions B, 2007, 38(5): 793−808.

[2] LI Mi, PENG Bing, CHAI Li-yuan, PENG Ning, XIE Xian-de, YAN Huan. Technological mineralogy and environmental activity of zinc leaching residue from zinc hydrometallurgical process [J]. Transactions of Nonferrous Metals Society of China, 2013, 23(5): 1480−1488.

[3] YU Da-wei, PAKTUNC D. Carbothermic reduction of chromite fluxed with aluminum spent potlining [J]. Transactions of Nonferrous Metals Society of China, 2019, 29(1): 200−212.

[4] YUAN Shuai, ZHOU Wen-tao, LI Yan-jun, HAN Yue-xin. Efficient enrichment of nickel and iron in laterite nickel ore by deep reduction and magnetic separation [J]. Transactions of Nonferrous Metals Society of China, 2020, 30(3): 812−822.

[5] LI Bo, WEI Yong-gang, WANG Hua. Non-isothermal reduction kinetics of Fe_2O_3−NiO composites for formation of Fe−Ni alloy using carbon monoxide [J]. Transactions of Nonferrous Metals Society of China, 2014, 24(11): 3710−3715.

[6] WANG Xin, YANG Da-jin, JU Shao-hua, PENG Jin-hui, DUAN Xin-hui. Thermodynamics and kinetics of carbothermal reduction of zinc ferrite by microwave heating [J]. Transactions of Nonferrous Metals Society of China, 2013, 23(12): 3808−3815.

[7] STOPIC S, FRIEDRICH B. Kinetics and mechanism of thermal zinc−ferrite phase decomposition [C]//Proceeding of EMC. Innsbruck, Austria, 2019: 1167−1181.

[8] LEE J J, LIN C I, CHEN H K. Carbothermal reduction of zinc ferrite [J]. Metallurgical and Materials Transactions B−Process Metallurgy and Materials Processing Science, 2001, 32(6): 1033−1040.

[9] JUNCA E, RESTIVO T A G, de OLIVEIRA J R, ESPINOSA D C R, TEN RIO J A S. Reduction of electric arc furnace dust pellets by simulated reformed natural gas [J]. Journal of Thermal Analysis and Calorimetry, 2016, 126(3): 1889−1897.

[10] JUNCA E, de OLIVEIRA J R, RESTIVO T A G, ESPINOSA D C R, TEN RIO J A S. Synthetic zinc ferrite reduction by means of mixtures containing hydrogen and carbon monoxide [J]. Journal of Thermal Analysis and Calorimetry, 2016, 123(1): 631−641.

[11] TONG L F, HAYES P. Mechanisms of the reduction of zinc ferrites in H_2/N_2 gas mixtures [J]. Mineral Processing and Extractive Metallurgy Review, 2006, 28(2): 127−157.

[12] TONG L F. Reduction mechanisms and behaviour of zinc ferrite. Part 2: $ZnFe_2O_4$ solid solutions [J]. Transactions of the Institution of Mining and Metallurgy Section C−Mineral Processing and Extractive Metallurgy, 2001, 110: C123−C132.

[13] TONG L F. Reduction mechanisms and behaviour of zinc ferrite. Part 1: Pure $ZnFe_2O_4$ [J]. Transactions of the Institution of Mining and Metallurgy Section C−Mineral Processing and Extractive Metallurgy, 2001, 110: C14−C24.

[14] WANG Zhong-bing, LIANG Yan-jie, PENG Ning, PENG Bing. The non-isothermal kinetics of zinc ferrite reduction

with carbon monoxide [J]. Journal of Thermal Analysis and Calorimetry, 2019, 136(5): 2157−2164.

[15] ALE EBRAHIM H, JAMSHIDI E. Kinetic study of zinc oxide reduction by methane [J]. Chemical Engineering Research and Design, 2001, 79(1): 62−70.

[16] LEW S, SAROFIM A F, FLYTZANI-STEPHANOPOULOS M. The reduction of zinc titanate and zinc oxide solids [J]. Chemical Engineering Science, 1992, 47(6): 1421−1431.

[17] CHEN Hsi−Kuei. Kinetic study on the carbothermic reduction of zinc oxide [J]. Scandinavian Journal of Metallurgy, 2001, 30(5): 292−296.

[18] PENG Bing, PENG Ning, MIN Xiao-bo, LIU Hui, CHAI Li-yuan, CHEN Dong, XUE Ke. Separation of zinc from high iron-bearing zinc calcines by reductive roasting and leaching [J]. JOM, 2015, 67(9): 1988−1996.

[19] GALWEY A K, BROWN M E. Thermal decomposition of ionic solids: Chemical properties and reactivities of ionic crystalline phases [M]. Elsevier, 1999.

[20] PENG Bing, PENG Ning, LIU Hui, XUE Ke, LIN Dong-hong. Comprehensive recovery of Fe, Zn, Ag and In from high iron-bearing zinc calcine [J]. Journal of Central South University, 2017, 24(5): 1082−1089.

锌焙砂的一氧化碳还原等温动力学

陈玉洁[1]，王云燕[1,2]，彭 宁[1,2,3]，梁彦杰[1,2]，彭 兵[1,2]

1. 中南大学 冶金与环境学院 环境工程所，长沙 410083；
2. 国家重金属污染防治工程技术研究中心，长沙 410083；
3. 中南大学 材料科学与工程学院，长沙 410083

摘 要：在 600~800 °C 温度范围通过等温还原焙烧方法研究锌焙砂的 CO 还原动力学。用热重法(TG)测定锌焙砂的反应程度，并根据可溶锌和亚铁含量的变化分析锌焙砂中铁酸锌的分解机理。结果表明，锌焙砂中铁酸锌的还原反应受产物的形核过程控制，表观活化能为 65.28 kJ/mol。与 CO 强度(定义为 $P_{CO}/(P_{CO}+P_{CO_2})$)相比，CO 的分压对反应速率的影响更大。在铁酸锌还原产物中，氧化锌的生成速率高于氧化亚铁的，表明氧化亚铁的形核过程为反应控制步骤。

关键词：还原动力学；锌焙砂；铁酸锌；一氧化碳

(Edited by Bing YANG)